



HAL
open science

Thermal properties of mid-infrared colloidal quantum dot detectors

Emmanuel Lhuillier, Sean E. Keuleyan, Rekemeyer Paul, Philippe Guyot-Sionnest

► **To cite this version:**

Emmanuel Lhuillier, Sean E. Keuleyan, Rekemeyer Paul, Philippe Guyot-Sionnest. Thermal properties of mid-infrared colloidal quantum dot detectors. *Journal of Applied Physics*, 2011, 110 (3), pp.033110. 10.1063/1.3619857 . hal-01438574

HAL Id: hal-01438574

<https://hal.science/hal-01438574v1>

Submitted on 25 Aug 2020

HAL is a multi-disciplinary open access archive for the deposit and dissemination of scientific research documents, whether they are published or not. The documents may come from teaching and research institutions in France or abroad, or from public or private research centers.

L'archive ouverte pluridisciplinaire **HAL**, est destinée au dépôt et à la diffusion de documents scientifiques de niveau recherche, publiés ou non, émanant des établissements d'enseignement et de recherche français ou étrangers, des laboratoires publics ou privés.

Thermal properties of mid-infrared colloidal quantum dot detectors

Emmanuel Lhuillier, Sean Keuleyan, Paul Rekemeyer and Philippe Guyot-Sionnest*

James Franck Institute, 929 E. 57th Street, The University of Chicago, Chicago, Illinois 60637,

USA

Keywords: Quantum dot, infrared, HgTe.

PACS: 85.35.Be, 85.60.Gz

Abstract

HgTe colloidal quantum dot films are studied for photodetection over the 3-5 μm atmospheric transparency window. The temperature dependence of the conductivity indicates that the material behaves approximately as an intrinsic semiconductor. In photoconduction, the responsivity can be as high as several hundred mA W^{-1} at room temperature. The dark current presents $1/f$ noise which is larger than for homogeneous conductors, and this noise decreases with temperature. A specific detectivity of 2×10^9 Jones is obtained for a sample with a 6 micron cut-off wavelength at 130K. These values are obtained for the thickest films studied (~ 400 nm) and whose thicknesses are still much less than the optical absorption length. The time response can be faster than 100 nanoseconds.

* To whom correspondence should be sent : pgs@uchicago.edu

18 I. INTRODUCTION

19 Colloidal quantum dots (CQD) have been studied over more than two decades, and they have
20 potential for various optoelectronic applications¹. While sharing the advantages of liquid
21 processing with organic molecular compounds, they have a very unique advantage in the infrared
22 due to weaker vibrational absorption and well defined infrared electronic absorption. They have
23 already been extensively investigated in the near-IR for photodetection,^{2,3,4,5,6}. PbS and PbSe
24 quantum dots are potential materials in the near-IR^{7,8,9,10}. For longer wavelengths, HgTe should
25 be a better choice since it is a gapless semiconductor^{5,11}. As CQD, this material had already been
26 shown to function well for near infrared photodetection^{12,13} and we recently extended the
27 material's response into the mid-IR.¹⁴

28 CQD may address current demand for a decrease of the cost of the infrared focal plane array and
29 an increase in operating temperature. Already established technologies in the mid infrared, such
30 as InSb or MCT or even promising detectors such as type II superlattices, achieve excellent
31 performances but fail to provide a low cost solution. In part, the high cost is due to the
32 requirement of epitaxial growth. HgTe CQD material can thus bring ease of processing and much
33 lower costs.^{15,16,17} Moreover the development of HgTe CQD benefits from the extensive
34 knowledge of HgCdTe, making this material easily transferable to MCT foundry.

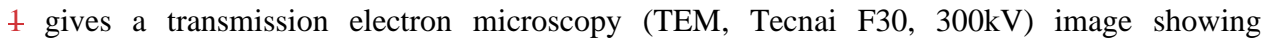
35 In this report we present an initial study of the temperature dependent conductivity and
36 photoconductivity characteristics of the HgTe CQD with mid-IR gaps. We report measurement of
37 the dark current, spectral response, responsivity and noise as a function of bias and temperature.
38 The efficiency of the CQD based detectors is evaluated and their optimal operating temperature
39 identified. We identify possible pathways for optimizing the material as a photodetector.

62

63 **II. EXPERIMENTAL**

64 **A. MATERIAL AND FILMS PREPARATION**

65 The synthesis of the QD particles uses the previously published method.¹⁴⁴⁰ Briefly, 13mg of
66 tellurium are dissolved in 2mL of butanol and 0.1mL of trioctylphosphine. The mixture is heated
67 to 90°C for 20 min under Ar to dissolve the tellurium. The temperature is then adjusted based on
68 the desired particle size, with higher temperatures leading to larger particles. The smallest
69 particles with band gaps reaching the visible region were obtained at temperatures as low as 0°C
70 while the largest particles were prepared at 90°C. Meanwhile mercury acetate is mixed with 2mL
71 of butanol and 2mL of pyridine. This solution is then quickly injected into the flask, immediately
72 forming a dark solution. Finally the reaction is stopped after several minutes by extracting to a
73 room temperature solution of 10% dodecanethiol in tetracholoethylene (TCE).

74 The diameters of the dots in this study are in the 6 to 12nm range. Particles with a ~8nm diameter
75 (respectively 10.5 nm) present a band edge energy corresponding to 3 μ m (5 μ m). [Figure 1](#)
76 [Figure](#)  gives a transmission electron microscopy (TEM, Tecnai F30, 300kV) image showing
77 aggregated particles. Dynamic light scattering (DLS, Malvern, Zetasizer) measurements suggest
78 the nanocrystals are similarly aggregated in colloidal solution. The aggregate size distribution
79 follows approximately a log normal distribution typical, with a mean size which is typically 20
80 times larger than the single dot diameter. However the optical absorption shows confinement
81 which varies only with the dimensions of the individual particles in the aggregates.

82 Films of dots are obtained by drop-casting the TCE CQD solution on interdigitated Pt electrodes
83 on a glass substrate (ABTech IME 1050, 50 periods, 100nm thick, 10 μ m width and spacing).

84 Films of HgTe CQD film studied here are a few hundred nanometers thick and we also
85 investigated thinner films made by using more dilute solutions. For all the following
86 measurements, the samples are mounted on the cold finger of a closed cycle He cryostat
87 (Coldedge SDRK 101D) operating between 3 and 300K. Three samples are under investigation in
88 this study with the following cut-off wavelength at room temperature 2.8 μ m (sample A), 3.4 μ m
89 (sample B) and 5.3 μ m (sample C).

90

91 **B. EXPERIMENTAL SETUP**

92 $I(V)$ curves are measured using a Keithley 6487 pico-ammeter. The sample is illuminated by a
93 tungsten light-bulb. Its temperature, measured with a pyrometer, is adjusted in the 1400 to
94 2100°C range, giving an incident power of a few mW on the sample.

95 A home-made Michelson interferometer is used to measure spectral responses. A SiC lamp
96 (equivalent to a 1200°C blackbody) serves as broadband light source and is chopped at a
97 frequency in the kHz range. The detector signal is amplified using a Keithley 6487 and a PAR
98 model 124 lock-in.

99 The transient response of the detector is obtained by illuminating the sample with short pulses
100 (10ps, 25Hz) of a Nd:YAG laser at 1.06 μ m. The transient photocurrent is recorded using a
101 100MHz digital oscilloscope (Tektronix, TDS 1012B).

102 Noise measurements are performed with a spectrum analyzer (HP 3561a). The sample is biased
103 with a battery in order to limit the input noise. The mean signal is removed using a resistor bridge
104 and the noise current is then input to a low noise operational amplifier (LF356N, National

120 Semiconductor). The current amplification is typically in the 10^4 to 10^7 range before input to the
121 spectrum analyzer. All the noise measurements were conducted in the cryostat with the optical
122 shutter closed.

123

124 III. RESULTS AND DISCUSSIONS

125

126 A. AN INTRINSIC SEMICONDUCTOR

127 Dark $I(V)$ curve for sample C are presented in ~~Figure 2~~Figure-2. The dark $I(V)$ curves present
128 almost no hysteresis. They are generally linear at high temperature and become less linear as the
129 temperature decrease. The dark current as a function of temperature is also presented in ~~Figure~~
130 ~~2~~Figure-2. The transport decreases about two orders of magnitude from the room temperature
131 value, with an Arrhenius law $I(T) \propto \exp\left(-\frac{E_a}{k_B T}\right)$, with E_a an activation energy, k_B the
132 Boltzmann constant, and T the temperature until settling to a lower slope. Activation energies are
133 reported in ~~Table 1~~Table-1 for sample A, B and C.

134

135

136 Table 1 : Activation energies for the dark current of the three samples. This value is compared to
 137 the half value of the optical gap at room temperature. N_0 is the estimated random close packed
 138 density of CQDs with the range based on a 20% standard deviation of the diameter. The carrier
 139 density, n , is estimated based on a model for intrinsic thermal activation. .

| Sample | $\lambda_{\text{cut-off}}$ (295 K) (μm) | $\lambda_{\text{cut-off}}$ (70K) (μm) | E_a (meV) | $E_G/2$ (meV) From optical measurement | N_0 ($\times 10^{18}$ cm^{-3}) | n ($\times 10^{16}$ cm^{-3}) | α (10^{-4} $\text{eV}\cdot\text{K}^{-1}$) | β (K) | $E_G(0\text{K})$ (eV) From Varshni's fit |
|---------------|---|--|-----------------|---|---|---|--|----------------|--|
| A | 2.8 | 3 | 273 ± 10 | 221 ± 44 | 2.6-7.6 | 0.08-0.3 | 1.5 | 500 | 0.43 |
| B | 3.4 | 4.35 | 201 ± 10 | 182 ± 36 | 1.5-5 | 0.2-0.8 | 7 | 500 | 0.33 |
| C | 5.3 | 6.6 | 106 ± 10 | 117 ± 20 | 0.6-2 | 1-4 | 7 | 500 | 0.23 |

140

141 The activation energy is in each case close to half of the energy gap value (at room temperature),
 142 the latter being determined as the edge of the photoresponse described below measured at room
 143 temperature. Such a relation between the energy of thermal activation of carriers and the gap is
 144 expected for an intrinsic semiconductor. At room temperature, we therefore conclude that the
 145 carrier density is dominated by the intrinsic properties. There may of course be some carrier
 146 doping in our samples, but given the thermal behavior of the dark current, it must be much less
 147 than the density of intrinsic carriers at room temperature. In the intrinsic case, the carrier density
 148 can be determined as $n = p = N_0 \sqrt{N_c \cdot N_v} \exp(-E_G / 2k_B T)$ where N_0 is the number of
 149 nanocrystals per volume, and N_c and N_v are the numbers of electron and hole states respectively
 150 in the nanocrystals that are thermally accessible. Given that much of the confinement energy is in
 151 the electron states, we take $N_c=2$. For the more massive holes, we will also take $N_v=2$ even

152 though it may be somewhat more. The estimated carrier densities at room temperature are then
153 shown in Table 1.

154 The measured resistivities of the samples allow an estimate of the mobility using $\rho^{-1} = ne\mu$,
155 which typically leads to value in the $0.5 \text{ cm}^2\text{V}^{-1}\text{s}^{-1}$ range for sample C. For the discussion later,
156 we also provide an estimate of the hopping time between nanocrystals. Using Einstein's relation,
157 the hopping time between nanocrystals and the mobilities are related by $\tau_{hop} \approx \frac{2eR^2}{3\mu k_B T} \approx 13 \text{ ps}$ in
158 sample C. Hopping times faster than recombination times are helpful for efficient operation.

159

160 **B. EFFECT OF THE TEMPERATURE ON THE OPTICAL PROPERTIES**

161 Figure 3 shows the spectral response for the three samples. By changing the size and temperature
162 of the particles, the cut-off wavelength tunes from 2.8 to almost 7 μm . Shorter cut-off
163 wavelengths are accessible by growing smaller particles but are not in the scope of this work. In
164 samples B and C, some features in the spectral response are due to vibrational absorption of the
165 C-H bonds from the ligands (3.5 μm), H₂O (3 μm) and CO₂ (4 μm) coming from water vapor and
166 carbon dioxide in the interferometer.

167 For all the samples, a decrease in temperature results in a red-shift of the spectral response, as
168 shown in ~~Figure 3~~ and ~~Table 1~~. This is consistent with bulk HgTe, where thermal
169 dilation of the HgTe lattice leads to a reduced gap with decreasing temperature.^{18,19}

170

171 The thermal dependence of the energy gap is captured quite well with an empirical parabolic fit.
172 Alternatively, Varshni's²⁰ expression, given by equation ~~(1)~~ (1), is often used.

$$173 \quad E_G(T) = E_G(T = 0K) + \frac{\alpha T^2}{\beta + T} \quad (1)$$

174 Here, the α parameter is linked to the thermal dilation coefficient. β was originally associated
175 with the Debye temperature although it can deviate significantly^{20,16}. The parameter values for
176 bulk HgTe are poorly known and reported values cover a wide range, with $\alpha = 2.7 \times 10^{-4} \text{ eV} \cdot \text{K}^{-1}$
177 to $8.5 \times 10^{-4} \text{ eV} \cdot \text{K}^{-1}$.^{18,14,19,15} Our experimental points are compared with a Varshni's law fit for
178 the thermal dependence. As shown in ~~Figure 2~~ Figure 2, the fit is imperfect and is in fact not very
179 sensitive to the choice of β , set at 500K, but the coefficient α is reasonable. Table 1 lists the
180 parameters. With more monodispersed samples it will be important to determine these parameters
181 with more accuracy than in the bulk and to extract their size dependence²¹ since the red shift with
182 temperature is relevant to the mid-IR detection.

183 Increasing the bias increases the magnitude of the response but it does not change its spectral
184 shape. The relative responsivity as a function of temperature is shown in Figure 4b and is
185 obtained by the integral of the photocurrent spectrum. At sufficiently high temperature, the
186 responsivity reaches a regime where it is independent of the detector temperature. However, at a
187 low enough temperature, the responsivity decreases exponentially.

188 The responsivity is proportional to the exciton ionization efficiency of a single dot multiplied by
189 the gain over the structure which is the ratio of the carrier lifetime over the carrier transit time,²²
190 as given by equation ~~(2)~~ (2).

191 $R \propto \eta \frac{\tau_{LT}}{\tau_{transit}} \quad (2)$

192 Future measurements of each of these parameters will be needed. At present we speculate that the
 193 ratio of carrier lifetime and transit times is a constant independent of temperature and bias. This
 194 will be the case if carrier trapping plays a significant role. A possible example of traps could be
 195 very large dots with therefore vanishing gaps. In this case, the major contributor to the
 196 temperature variation of R is the ionization efficiency η . We then consider that the ionization rate
 197 is thermally activated $k_i = k_{i0} \exp(-E/k_b T)$ and competes with a fixed recombination rate k_r
 198 due to radiative and nonradiative processes within one dot. The ionization efficiency is then

199 $\eta_{\text{single QD}} = \frac{e^{-E_i/kT}}{k_r/k_{i0} + e^{-E_i/kT}} \quad (3)$

200 Fitting the experimental data with such an expression leads to a strong discrepancy at the lowest
 201 temperature since it predicts $\eta = 0$ at 0K. Such a deviation may result from the distribution of
 202 activation energies. For a collection of dots, we choose a Gaussian energy distribution such that

203 $\eta_{\text{ensemble}}(T, E_i, \sigma) = \int_{-\infty}^{\infty} \eta_{\text{single QD}}(T, E) \frac{1}{\sigma\sqrt{2\pi}} \exp\left(-\frac{(E - E_i)^2}{2\sigma^2}\right) dE \quad (4)$

204 This provides a better fit with values of the mean activation energies of 160meV for sample A,
 205 100 meV for sample B and 34 meV for sample C. The broadening of the ionization energies are
 206 within 20-50%. In this model, the saturation of the ionization efficiency at moderate temperature
 207 implies that the time required for charge separation becomes smaller than the recombination time,
 208 radiative and non-radiative, and therefore that the quantum yield of charge generation is already

209 close to unity. This is compatible with the fast hopping time mentioned earlier at room
210 temperature.

211 The origin of these activation energies for charge separation may lie in the disorder associated
212 with the size inhomogeneity and in an energy barrier associated with charge transfer, even in the
213 absence of disorder. To estimate the latter, we use Marcus theory²³ considering that the electron
214 (or hole) transfers from an exciton in a sphere with binding energy E_{ex} to a neighboring sphere.

215 The Exciton binding energy is given by²⁴ $E_{ex} = 1.8 \frac{e^2}{\epsilon R}$, with R the radius of the dot and ϵ their
216 dielectric constant. Assuming a value of $\epsilon=20$ in HgTe^{25,26}, this is estimated as 32 meV and 24
217 meV for samples B ($R=4$ nm) and C ($R=5.3$ nm). The Marcus expression for the energy barrier is

218 $\Delta G_0 = \frac{\lambda_0}{4} (1 + \frac{E_{ex}}{\lambda_0})^2$ where λ_0 is the reorganization energy. For electron transfer in a two-sphere

219 model $\lambda_0 = e^2 \left(\frac{1}{R} - \frac{1}{R + \delta} \right) \left(\frac{1}{\epsilon_\infty} - \frac{1}{\epsilon_0} \right)$, where R is the dot radius, and δ is the matrix thickness

220 between the dot surfaces estimated as ~ 1 nm for the dodecanethiol. The dynamic and static
221 dielectric constants, ϵ_∞ and ϵ_0 , refer to the matrix. This is unknown for the matrix material,
222 mostly bound alkane thiol, but we take $\epsilon_\infty = 2.1 \ll \epsilon_0$. This gives energy barriers of 32 meV and
223 25 meV for samples B and C respectively. Energy disorder due to size inhomogeneity could
224 easily be a larger effect, and may explain the discrepancy with measured values above.

225

226 C. RESPONSIVITY

227 Using the $I(V)$ curves under illumination, as described in reference [1410](#), we can extract the
228 absolute responsivity of our detectors. To proceed, we first identify a temperature at which the

246 dark current is far below the photocurrent in our range of flux (room temperature for the A
 247 sample, 190K for the C sample). We then measure two $I(V)$ curves under illumination at this
 248 temperature, for two different amounts of incident flux. This latter is evaluated as in equation

249 ~~(3)~~ ~~(3)~~

$$250 \quad \phi(T_{BB}, \alpha, \beta) = A_d \pi \cdot \cos \beta \cdot \sin^2 \alpha \int_{\lambda_{\min}}^{\lambda_{\text{cutoff}}} \frac{2hc^2}{\lambda^5} \frac{1}{e^{\frac{hc}{\lambda k T_{BB}}} - 1} d\lambda, \quad (3)$$

251 Where A_d is the active area of the sample (0.1 cm^2), α is the half angle of view of the detector and
 252 β is the angle between the normal of the detector and the incident light, h is the Planck constant, c
 253 the speed of the light, and T_{BB} the equivalent black-body temperature of the light source.

254 Finally the responsivity is given by equation ~~(4)~~ ~~(4)~~

$$255 \quad R = \frac{I_{\text{total}}(\phi_1) - I_{\text{total}}(\phi_2)}{\phi_1 - \phi_2} \quad (4)$$

256 We thus obtained the absolute responsivity at one temperature and the relative responsivity in
 257 ~~Figure 4~~ ~~Figure 4~~ (b), for the other temperatures. Finally the responsivity as a function of the
 258 applied bias is plotted in ~~Figure 5~~ ~~Figure 5~~. The responsivity appears linear with bias.

259 **D. NOISE AND DETECTIVITY**

260 The spectrum analyzer provides the voltage noise density (v_n). The current noise density (i_n)
 261 which is the useful quantity to evaluate the detectivity, is then obtained by $i_n = \frac{v_n}{G \cdot BW}$, where G
 262 is the current amplification and BW is the bandwidth of the spectral acquisition.

Mis en fo
 Mis en fo

283 The noise for sample C is plotted in ~~Figure 6~~Figure-6 (a) and (b). At all biases and temperatures,
284 a non-white noise prevails at low frequency, and follows a power law with an exponent in the -
285 0.4 to -0.7 range consistent with $1/f$ noise. As temperature and bias increase, the dark current and
286 the noise both increase.

287

288 $1/f$ noise can be modeled using the Hooge's law²⁷,

289
$$i_{1/f}^2 = \frac{\alpha_H \cdot I^2}{N \cdot f} \quad (5)$$

290 where N is the number of carriers, I the average current through the sample, f the frequency and
291 α_H is a parameter which describes the magnitude of the $1/f$ noise. Hooge reported that in most
292 metallic materials, this parameter is rather close to 2×10^{-3} . While we do not know of reported
293 values of α_H for bulk HgTe, α_H has a value in the 10^{-3} to 10^{-5} range for HgCdTe detectors^{28,29}
294 (with a cadmium content in in the 0.17 to 0.3 range), also much smaller than observed here. We

295 extract $\frac{\alpha_H}{N} = f \frac{i_{1/f}^2}{I^2}$, shown in ~~Figure 6~~Figure-6 (c) for $f=10\text{Hz}$. The number of carriers can be

296 evaluated as the product of the carrier density, which was estimated in table 1, and the volume of

297 the sample. This gives 4×10^{10} carriers for sample C. Since the value of $\frac{\alpha_H}{N}$ is typically 10^{-11} for

298 sample C, α_H is therefore around 0.4, two decades above the Hooge value. The larger value of

299 the Hooge constant therefore suggests that our CQD samples are possibly about 10 fold noisier

300 than they need to be. One possibility is that the sample inhomogeneity induces current

301 crowding^{30,31} such that the actual number of carriers should not be related to the total volume of

302 the sample. Whether the noise level is intrinsically related to the nanoparticle assembly or more

323 specific of the particular samples that we have studied, and in particular the aggregation
324 discussed in section I, Figure 1, remains unknown and is a target of further study.

325 Finally, by combining the responsivity and noise measurements we evaluate the specific
326 detectivity of the samples, using equation ~~(6)~~(6).

$$327 \quad D^* = \frac{R\sqrt{A_d}}{i_n} \quad (6)$$

328 Maps of the detectivity as a function of the operating temperature and applied bias are presented
329 in ~~Figure 7~~Figure 7.

330 These maps show that the HgTe CQD material is able to reach detectivity above 10^9 Jones. The
331 optimal operating temperature is just below room temperature (270K) for sample A ($\lambda_{cut-off} =$
332 $2.8\mu\text{m}$) and is around 130K for sample C (with a $\lambda_{cut-off} \approx 6\mu\text{m}$ at this temperature). The applied
333 optimal biases are respectively for sample A and C 19V (corresponding to an electric field of
334 8kV cm^{-1}) and 8V (19kV cm^{-1}), which is above the applied bias of the regular read-out circuit
335 (generally a few volts). Nevertheless this optimal bias can easily be reduced by changing the
336 spacing of the electrodes.

337

338 E. INFLUENCE OF THE THICKNESS

339 The thickness of the CQD film is an important parameter determining some of the detector
340 properties. In particular, based on bulk optical properties of HgTe, the absorption depth of films
341 of CQDs is expected to be around 5 microns, which is an order of magnitude larger than the
342 thickest samples studied. Correspondingly, the optical densities of the samples were rather small,

357 of the order of 0.1. Thicker films will directly lead to improved responsivities. While making
 358 uniform thick films will require a dedicated effort, it is interesting to explore how the response of
 359 thinner films varies with thickness. Therefore, three samples based on sample C of respective
 360 thickness 15, 35 and 450nm have been studied. Their properties are summarized in [Table 2](#)
 361 [2](#). The thickness is measured using an Atomic Force Microscope, scanning a groove made with a
 362 sharp razor blade.

363 Table 2: Properties of the three films based on sample C ($\lambda_{\text{cut-off}} \approx 5\mu\text{m}$) and of different
 364 thicknesses. The time response is the 1/e decay time.

| | Thick film | Medium film | Thin film |
|---|-------------------|--------------------|------------------|
| Appearance | Brown | Barely colored | Colorless |
| Thickness (nm) | 450 | 35 | 15 |
| Dark Current, at 10V (mA) | 22 | 0.56 | 0.031 |
| Resistance (room T) at 10V (k Ω) | 0.5 | 17 | 320 |
| Responsivity (normalized by thick film value) | 1 | 7% | 0.2% |
| Decay time (ns) | 63 | 2×10^3 | 5×10^5 |

365

366 Even the thinnest film provides a measurable mid-IR photoresponse, while being very transparent
 367 and only a couple layers of dots. Generally the thicker the film the smaller the resistance, see
 368 [Figure 8](#) [Figure 8](#) (a). An increase of the thickness also results in greater absorption which leads to
 369 a higher responsivity ([Figure 8](#) [Figure 8](#)(c)). In parallel, the noise also increases with sample
 370 thickness. According to Hooge's expression, we expect the current $1/f$ noise to increase as the

Mis en fo

393 square root of thickness while the responsivity increases linearly with the thickness as long as it
394 remains much smaller than the absorption length. Therefore, there should be a net increase of the
395 detectivity with square root of the thickness. A square root fit is then used as a guide to the eye in
396 [Figure 8](#) [Figure 8](#) (e).

397 The measurement of the transient photocurrent has been used to probe the density of states inside
398 the gap of several materials.^{32,33} Here, we focus on the transient photocurrent decay, which is
399 related to the cut-off frequency of the detector. Surprisingly, an increase in film thickness gives a
400 faster response of the detector, see [Figure 8](#) [Figure 8](#) (b). It is also observed that an increase of the
401 bias leads to a faster response, both for the rise and decay time while the incident beam energy
402 only slightly affects the transient shape. Increasing the operating temperature of the detector,
403 from 250K to 295K, also leads to a faster response. While these effects are not completely
404 understood, they likely arise from capacitance associated with space charge at the contacts³⁴.
405 While this capacitance is constant for a given electrode geometry, the resistance of the devices
406 drops with increasing film thickness, bias and temperature, leading to a decreased RC time
407 constant. Compared to PbS CQD detector⁹ operating in the near-IR, the HgTe times response are
408 much faster but the responsivities are also lower, in accordance with equation [\(2\)](#).

409
410 Since the optimal detectors need to have thicknesses larger than the thickest one studied here in
411 order to saturate the absorption, we expect that the speed of the detector will be much faster than
412 required for usual imagery application for which the typical integration time is in the 1ms range.

413

414 IV. CONCLUSION

Mis en fo

415 The conductivity and mid-infrared response photoconductivity of HgTe CQD solid films are
416 investigated as a function of temperature. By changing the size of the particle and the
417 temperature, the cut-off wavelength has been tuned from the near infrared up to $7\mu\text{m}$. The
418 measured responsivity already competes with existing devices such as QWIP³⁵ or type II
419 superlattices^{36,37} and further improvements are expected with optimized thicker films.

420 The dark current is thermally activated with an activation energy close to half of the energy gap.
421 This suggests that, at room temperature, most carriers are thermally generated. From the
422 estimated carrier density, the mobility is extracted and is relatively large at room temperature, of
423 the order of $0.1\text{-}1\text{ cm}^2\text{V}^{-1}\text{s}^{-1}$, especially given that the material is a simple drop-cast film of CQDs
424 without any attempt to eliminate or replace the ligands. These mobility values will need to be
425 confirmed by direct measurements. We observe that the temperature dependence of the
426 responsivity is much weaker than that of the dark current, being essentially constant around room
427 temperature and dropping only at lower temperatures. We interpret this behavior as arising from
428 already efficient charge separation at room temperature. The films show $1/f$ noise at low
429 frequency with values of the Hooge's constant that are two orders of magnitude larger than for
430 clean homogeneous metals, although the noise decreases with temperature leading to an optimum
431 operating temperature. The best detectivity values for a 450 nm thick film are $\sim 2\times 10^9$ jones at
432 130K and the fastest response times are below 100 ns at room temperature. We stress again that
433 these results have been obtained with no processing of the films other than simply drop-cast from
434 solutions.

435 Since the mobility and carrier generation efficiency are already high it seems that further
436 improvement will rather come from the improved optical absorption edge, longer carrier lifetime,
437 and reduced noise. Improved optical properties come from thicker films, and materials with

438 improved monodispersivity. Higher monodispersivity will also reduce the concentration of large
439 dots which may act as recombination centers. Reducing the noise will involve investigating the
440 effect of film processing to possibly reduce the crowding effect which maybe the source of
441 excess $1/f$ noise. It is expected that detectivities above 10^{10} Jones in the mid-IR will be achievable
442 while maintaining a fast response time and moderate cooling temperatures consistent with
443 imaging operation.

444

445 **V. ACKNOWLEDGEMENTS**

446 The research was supported by the US National Science Foundation NSF under Grant No
447 DMR-070626 and by DOE under Grant No. DE-FG02- 06ER46326. The authors made use of
448 shared facilities supported by the NSF MRSEC Program under DMR-0820054. EL thanks Ecole
449 Polytechnique, Palaiseau, France, for a postdoctoral fellowship.

450

451
452 Figure 1: (a) TEM image of the HgTe material. (sample C) Scale bar is 10 nm. The inset shows a
453 high resolution image of a single dot. (b) Diameter distribution of single dots for sample C
454 measured from TEM imaging (c) Hydrodynamic radii distribution in solution (sample C)
455 obtained by dynamic light scattering (DLS), and a log normal fit of the distribution with a 220
456 nm mean value.

457
458 Figure 2: Dark current for sample C, as a function of the inverse of the temperature, for three
459 different biases. The inset shows the $I(V)$ curve for the sample C for two different temperatures.

460
461 Figure 3: Normalized spectral response for the sample A (top), B (middle) and C (bottom) for
462 different temperatures. These spectra have been acquired while the samples were respectively
463 biased by 2V, 1V and 0.3V.

464
465 Figure 4 (a) Position of the long-wavelength half maximum of the spectral response as a function
466 of the temperature for the sample C. (b) Relative responsivity (integral of the photocurrent
467 spectrum), normalized to the room temperature value as a function of temperature for samples A,
468 B and C. The solid lines are associated fit as discussed in the text.

469

470 Figure 5: Responsivity for samples A, B and C as a function of the applied bias for different
471 temperatures.

472

473 Figure 6: (a) Current noise spectral density for a 2V bias at temperatures: 70, 110, 150, 190, 230,
474 250 and 295K for sample C. (b) Current noise spectral density at 250K at applied bias: 0.5, 2 and
475 5V for sample C. (c) Ratio of the α_H Hooge's parameter over the number of carriers as a function
476 of the detector temperature at 10V for sample C at 10Hz.

477

478 Figure 7: Map of the specific detectivity as a function of temperature and applied bias for sample
479 A (top) and C (bottom).

480

481 Figure 8: (a) Dark current as a function of the applied voltage for three films. (b) Transient
482 photocurrent in response to a short (10ps) laser pulse of 1.06 μ m wavelength, with 7V bias (c)
483 Relative responsivity as a function of the applied bias, (d) noise current spectral density, at a 7V
484 bias and (e) Detectivity (at 7V) as a function of film thickness for three films of different
485 thicknesses based on the material of sample C. All measurements were conducted at room
486 temperature. In the graphs a, b, c, d, the solid line is for the 15nm film, the dashed line for the
487 35nm film and the dotted line for the 450nm film.

488

490 VI. REFERENCES

-
- ¹ For a recent review see D. Talapin, J.S. Lee, M. Kovalenko and E. Shevchenko, *Chem. Rev.* **110**, 389 (2010).
- ² G.I. Koleilat, L. Levina, H. Shukla, S.H. Myrskog, S. Hinds, A.G. Pattantyus-Abraham, E.H. Sargent, *ACS Nano.* **2**, 833 (2008).
- ³ J. Tang, E. H. Sargent, *Advanced Materials* **23**, 12 (2011).
- ⁴ I. M Tsidilkovski, *Electron spectrum of gapless semiconductors*, Springer series on solid state sciences 116, Springer, Heidelberg, 1997.
- ⁵ G. Nimtz and B. Schlicht, *Narrow-gap semiconductors*, Springer tracts in modern physics 98, Springer, Heidelberg, 1983.
- ⁶ T. Rauch, M. Böberl, S. F. Tedde, J. Fürst, M. V. Kovalenko, G. Hesser, U. Lemmer, W. Heiss, O. Hayden, *Nature Photonics* **3**, 332 (2009)
- ⁷ E. H. Sargent, *Adv. Mater.* **17**, 515 (2005).
- ⁸ G. Konstantatos, C. Huang, L. Levina, Z. Lu and E. H. Sargent, *Adv. Func. Mater.* **15**, 1865 (2005).
- ⁹ G. Konstantatos, I. Howard, A. Fischer, S. Hoogland, J. Clifford, E. Klem, L. Levina and E. H. Sargent, *Nature* **442**, 180 (2006).
- ¹⁰ J. M. Pietryga, R. D. Schaller, D. Werder, M. H. Stewart, V. I. Klimov, and J. A. Hollingsworth, *J. Am. Chem. Soc.* **126**, 11752 (2004).
- ¹¹ I. M Tsidilkovski, *Electron spectrum of gapless semiconductors*, Springer series on solid state sciences 116, Springer, Heidelberg, 1997.
- ¹² M. Kovalenko, E. Kaufmann, D. Pachinger, J. Roither, M. Huber, J. Stangl, G. Hesser, F. Schaffler, and W. Heiss, *J. Am. Chem. Soc.* **128**, 3516 (2006).
- ¹³ M. Böberl, M. V. Kovalenko, S. Gamerith, E. J. W. List, and W. Heiss, *Advanced Materials* **19**, 3574 (2007).
- ¹⁴ S. Keuleyan, E. Lhuillier, V. Brajuskovic and P. Guyot-Sionnest, *Mid-infrared HgTe colloidal quantum dot photodetectors*, submitted to *Nat. Photonics* (2011).
- ¹⁵ L. Kim, P. O. Anikeeva, S. A. Coe-Sullivan, J. S. Steckel, M. G. Bawendi and V. Bulovic, *Nano Lett* **8**, 4513 (2008).
- ¹⁶ V. Wood, M. J. Panzer, J. Chen, M. S. Bradley, Jonathan E. Halpert, M. G. Bawendi, V. Bulović, *Advanced Materials* **21**, 2151 (2009).
- ¹⁷ T. Kim, K.Cho, E. K. Lee, S. J. Lee, J. Chae, D. H. Kim, J. Kwon, G. Amaratunga, S. Y. Lee, J. Kim , B. L. Choi, Y. Kuk , J. M. Kim and K. Kim, *Nat. Photonic* **5**, 176 (2011).
- ¹⁸ C. S. Guenzer and A. Bienenstock, *Phys. Rev. B* **8**, 4655 (1973).
- ¹⁹ M. Dobrowolska, A. Mycielski and W. Dobrowolski, *Solid State Comm.* **27**, 1233 (1978).
- ²⁰ Y. P. Varshni, *Physica* **34**, 149 (1967).
- ²¹ A. Olkhovets, R.-C. Hsu, A. Lipovskii, and F. W. Wise, *Phys. Rev. Lett.* **81**, 3539 (1998).
- ²² E. Rosencher and B. Vinter, in *Optoelectronics (Cambridge University Press, Cambridge, 2002)*.
- ²³ R.A. Marcus, *Pure and Appl. Chem.* **69**, 13 (1997)
- ²⁴ L. E. Brus, *J. Chem. Phys.* **79**, 5566, (1983).

²⁵ K. Ortner, X. C. Zhang, A. Pfeuffer-Jeschke, C. R. Becker, G. Landwehr, and L. W. Molenkamp, *Phys. Rev. B* **66**, 075322 (2002).

²⁶ V. Radhakrishnan and P. C. Sharma, *Phys. Rev. B* **23**, 3004 (1981).

²⁷ F. N. Hooge, *IEEE Trans. Elec. Devices* **41**, 1926 (1994).

²⁸ R.J. Westerhout, C.A. Musca, J. Antoszewski, J.M. Dell and L. Faraonen, *J. Electronic Materials* **36**, 884 (2007).

²⁹ C.T. Elliot, N.T. Gordon, R.S. Hall, and T.J. Phillips, C.L. Jones and A. Best, *J. Electronic Materials* **26**, 643 (1997).

³⁰ E.P. Vandamme and L.K.J. Vandamme, *Microelectronics reliability* **40**, 1847 (2000).

³¹ A. Mercha, L.K.J. Vandamme, L Pichon, R carin and O. Bonnaud, *J. Appl. Phys.* **90**, 4019 (2001).

33

A. Rose, *Phys. Rev.* **97**, 1538 (1954).

³⁵ V. Guériaux, A. Nedelcu and P. Bois, *J. Appl. Phys.* **105**, 114515 (2009).

³⁶ E. Plis, J.B. Rodriguez, G. Balakrishnan, Y.D. Sharma, H.S. Kim, T. Rotter and S. Krishna, *Semicond. Sci. Technol.* **25**, 085010 (2010).

³⁷ M. Walther, R. Rehm, F. Fuchs, J. Schmitz, J. Fleissner, W. Cabanski, D. Eich, M. Finck, W. Rode, J. Wendler, R. Wollrab and J. Ziegler, *J. Elec. Mat.* **34**, 722 (2005).